

张静, 许乃岑, 沈加林, 等. 稀土元素铽镧掺杂对硫氧化钆晶格场的影响及发光性能研究[J]. 岩矿测试, 2025, 44(2): 254–267.  
DOI: [10.15898/j.ykcs.202405070105](https://doi.org/10.15898/j.ykcs.202405070105).

ZHANG Jing, XU Naicen, SHEN Jialin, et al. Influence of Rare Earth Terbium and Lanthanum Doping on the Lattice Field and Luminescence Performance of Gadolinium Oxysulfide[J]. Rock and Mineral Analysis, 2025, 44(2): 254–267. DOI: [10.15898/j.ykcs.202405070105](https://doi.org/10.15898/j.ykcs.202405070105).

## 稀土元素铽镧掺杂对硫氧化钆晶格场的影响及发光性能研究

张静<sup>1,2</sup>, 许乃岑<sup>1</sup>, 沈加林<sup>1\*</sup>, 金凡<sup>1</sup>

(1. 中国地质调查局南京地质调查中心, 江苏南京 210016;  
2. 南京工业大学, 江苏南京 211816)

**摘要:** 稀土硫氧化物具有较好的传能效率、热稳定性和化学稳定性, 其作为发光材料的基质被广泛应用于防伪、显示器、发光二极管、医学影像等领域。由于硫氧化钆( $\text{Gd}_2\text{O}_2\text{S}$ )的晶体空间结构较宽, 当间隙离子进入其中, 或阳离子、阴离子形成空位时, 晶体结构也依然保持不变。但硫氧化钆荧光粉容易发生团聚现象, 使得样品颗粒尺寸较大, 降低了样品颗粒的堆积密度, 提高了能量的散射率, 导致获得的光不均匀。用于显示设备时, 粉末粒径大会导致在同一视域里像素数量较少, 分辨率较差。本文以 $\text{Gd}_2\text{O}_2\text{S}$ 为研究对象, 采用硫熔法制备了硫氧化钆荧光粉, 引入稀土离子 $\text{Tb}^{3+}$ 、 $\text{La}^{3+}$ 作为掺杂离子, 通过优化稀土离子的掺杂量, 获得结晶度高、分散性好、尺寸均匀性相对较好的 $\text{Gd}_2\text{O}_2\text{S}$ 基荧光粉。利用荧光分光光度计、X射线衍射(XRD)等测试技术, 探讨稀土掺杂对 $\text{Gd}_2\text{O}_2\text{S}$ 晶格场的影响及发光性能的影响。XRD结果表明: ①荧光粉为纯六方晶体结构; ② $\text{Tb}^{3+}$ 、 $\text{La}^{3+}$ 替代 $\text{Gd}^{3+}$ 进入 $\text{Gd}_2\text{O}_2\text{S}$ 的晶格位置。荧光粉的荧光光谱图显示: ①掺入 $\text{Tb}^{3+}$ 后, 在544nm处会发生 $^5\text{D}_4 \rightarrow ^7\text{F}_5$ 的浓度猝灭, 是由于电偶极-电偶极跃迁引起的; ②发光强度在 $\text{Tb}^{3+}$ 掺杂浓度为2mol%时最大; ③ $\text{La}^{3+}$ 的掺杂增强了硫层的电负性, 所以随着掺杂量的增加, 晶胞之间的排斥力也逐渐增强, 晶粒尺寸逐渐减小, 发光强度也随之增强; ④当 $\text{La}^{3+}$ 掺杂浓度为60mol%时, 发光强度为未掺杂 $\text{La}^{3+}$ 样品的1.9倍。本文通过计算电多级级数分析离子间能量转移的过程, 从而确定了发光材料 $\text{Tb}^{3+}$ 、 $\text{La}^{3+}$ 的最佳掺杂浓度。

**关键词:** 发光; 稀土离子掺杂; 硫氧化钆; 荧光分光光度计法; X射线衍射法

### 要点:

- (1) 用硫熔法制备 $\text{Tb}^{3+}$ 掺杂的 $\text{Gd}_2\text{O}_2\text{S}$ 荧光粉, 研究了 $\text{Tb}^{3+}$ 的掺杂浓度对 $\text{Gd}_2\text{O}_2\text{S}$ 发光性能的影响。
- (2) 引入稀土离子 $\text{La}^{3+}$ 取代 $\text{Gd}_2\text{O}_2\text{S}$ 中的基质离子 $\text{Gd}^{3+}$ , 使得 $\text{Tb}^{3+}$ 周围的晶格场环境发生改变, 有效地提高了 $\text{Gd}_2\text{O}_2\text{S}$ 的荧光性能。
- (3) 探讨 $\text{Tb}^{3+}$ 以及 $\text{La}^{3+}$ 在 $\text{Gd}_2\text{O}_2\text{S}$ 基体中的能量转移机制, 分析稀土离子掺杂对 $\text{Gd}_2\text{O}_2\text{S}$ 荧光粉的作用机理。

中图分类号: P575

文献标识码: A

特殊的4f亚层电子排布<sup>[1]</sup>和强大的自旋轨道相互作用力, 以及较大的原子磁场强度等因素使得

稀土金属展现了丰富的光学、电气与物理属性特征。当它们的4f壳层中的电子数量发生变化时, 会产生

收稿日期: 2024-05-07; 修回日期: 2024-09-23; 接受日期: 2024-09-26; 网络出版日期: 2024-11-13

基金项目: 中国地质调查局地质调查项目“苏皖沿江凹陷带油气页岩气调查评价”(DD20221662); 中国自然科学基金联合基金重点项目“浙闽火山岩区蚀变岩帽叶腊石和明矾石矿物指针研究”(U23442091); 中国地质调查局南京地质调查中心成果转化项目“月球及火星模拟样品矿物组成研究”(NJZXK2023-034)

第一作者: 张静, 博士研究生, 助理研究员, 主要从事矿物(材料)结构分析和矿物功能材料研究。

E-mail: [lavenderesta@126.com](mailto:lavenderesta@126.com)。

通信作者: 沈加林, 硕士, 正高级工程师, 主要从事分析测试和地质矿产研究。E-mail: [sjlilu@163.com](mailto:sjlilu@163.com)。

显著且多样化的能量转移现象,这使稀土元素能够吸收或发射覆盖整个可见光范围内的不同颜色的光<sup>[2]</sup>,而这种卓越的能力为制备高性能的荧光粉提供了可能的基础条件<sup>[3-5]</sup>。由于稀土硫氧化物独特的层状构造、低至约500cm<sup>-1</sup>的声子能量,使其展现出极高的熔点(通常2000~2200℃)<sup>[6]</sup>,同时拥有较窄的禁带宽度(大约4.6~4.8eV)<sup>[7]</sup>,这使得它具备了高度的化学和热稳定性,因此经常作为荧光粉的基质材料<sup>[8-9]</sup>。这种由稀土硫氧化物制成的发光材料因其卓越的光吸收及传递性能而备受关注<sup>[10-12]</sup>,并被成功应用于光电子器件、磁性材料、催化剂等领域<sup>[13-15]</sup>。

稀土硫氧化物具有六方晶体结构,它的化学键表现为共价键-离子键的混合态,空间群归属P3ml,并且拥有较为宽敞的空间架构,这便能容纳一定数量的间隔离子进入,同时也能产生阳阴离子的空缺,使其晶体结构仍可维持相对稳定<sup>[16]</sup>。近年来,研究者们对稀土硫氧化物的制备方法、物理化学性能进行了大量研究,发现稀土硫氧化物的颗粒形貌、颗粒尺寸、原料配比、热处理温度、助熔剂选择等都对其发光性能有影响<sup>[17-18]</sup>。Qian等<sup>[19]</sup>通过水热法制备了Tb<sup>3+</sup>、Sm<sup>3+</sup>掺杂的Gd<sub>2</sub>O<sub>2</sub>S荧光粉。荧光粉呈现胶囊状,具有六方晶相结构和良好的发光性能。通过改变掺离子浓度和激发波长,可以实现从绿光到橙红光的各种颜色的可调发光。Jiang等<sup>[20]</sup>通过调节溶液pH值,合成了片状、球形、扁方形、长方体以及棒状的Tb<sup>3+</sup>掺杂的Gd<sub>2</sub>O<sub>2</sub>S荧光粉。结果表明,所有形态的荧光粉均为纯六方相。随着形态的变化,荧光粉的带隙能从3.76eV变为4.28eV,可以观察到带隙能呈现逐渐增加的趋势,发光性能也随之不同。相较之下,具有球状和立方体微结构的荧光粉表现出更为优异的发光性能,并且所得荧光粉的发射颜色受激发源的强烈影响。Machado等<sup>[21]</sup>探索了利用快速微波辅助固相法(MASS)合成了一系列Er<sup>3+</sup>掺杂的Gd<sub>2</sub>O<sub>2</sub>S荧光粉以及Er<sup>3+</sup>、Yb<sup>3+</sup>掺杂的Gd<sub>2</sub>O<sub>2</sub>S荧光粉。使用两种不同的起始化合物,稀土氧化物(Ln<sub>2</sub>O<sub>3</sub>)和羟基碳酸盐[Ln(OH)CO<sub>3</sub>],其中Ln为Gd、Er、Yb,结果表明,使用Ln(OH)CO<sub>3</sub>替代更常见的Ln<sub>2</sub>O<sub>3</sub>进行MASS合成,有助于Er<sup>3+</sup>和Yb<sup>3+</sup>在Gd<sub>2</sub>O<sub>2</sub>S基体中的均匀分布,同时得到更优异的上转换发光性能。MASS法与传统固相方法相比,制备时间减少79%,能耗减少93%。目前常用的制备方法有:  
①高温固相法,优点是操作简单、产量高,但易引入杂质且粒径较大;  
②水热法,优点是分散性好,但需

要在高压下操作且产量较低;  
③溶胶凝胶法,优点是样品纯度好,但成本高且对环境有一定危害;  
④燃烧法,优点是快速、粒径较小,但发光强度较低且会产生烟雾;  
⑤微乳液法,优点是粉末结晶度好,但成本较高且引入表面活性剂会影响发光性能;  
⑥硫熔法,优点是操作过程简单、粉体发光效率高,但样品容易团聚,这样获得的样品颗粒尺寸较大,降低了样品颗粒的堆积密度,提高了能量的散射率,导致获得的光不均匀。用于显示设备时,粉末粒径大会导致在同一视域里像素数量较少,分辨率较差。

如何获得粒径较小、窄分布、发光强度高的硫氧化钆荧光粉是硫熔法制备方法的关键。本文以Gd<sub>2</sub>O<sub>2</sub>S作为基体,首先采用硫熔法制备Tb<sup>3+</sup>掺杂的Gd<sub>2</sub>O<sub>2</sub>S荧光粉。利用X射线衍射仪分析样品的物相组成与结构,荧光分光光度计测量样品的发射光谱和激发光谱,进一步探讨Tb<sup>3+</sup>的掺杂浓度对荧光粉的晶格场环境和发光特性的影响。在制得发光效率较高的Tb<sup>3+</sup>单掺杂的Gd<sub>2</sub>O<sub>2</sub>S荧光粉后,以稀土离子La<sup>3+</sup>部分取代Gd<sup>3+</sup>,通过引入稀土掺杂离子,来有效地提升荧光粉的发光强度,探讨其对荧光粉的晶格场环境以及发光性能的影响。最终,制得粒径较小、窄分布、发光强度高的硫氧化钆荧光粉。

## 1 实验部分

### 1.1 稀土荧光粉的制备

实验流程如图1所示,按照化学计量比称取物料(氧化钆、升华硫、无水碳酸钠、氧化铽、氧化镧),将物料与玛瑙球混合,置于球磨机上,球磨10h,使物料充分混合均匀。混合物料干燥后,采用双坩埚套埋的方式,在高温程序炉中进行煅烧。热处理温度设置为从室温加热到270℃,保温1h,再升温到1100℃保温3h,升温速率设为5℃/min。自然冷却后,把经过煅烧的粉末放入烧杯中,用去离子水洗涤三遍,将洗涤完成的粉末进行抽滤。重复洗涤、抽滤三遍后,将样品放入干燥箱中,在80℃下烘干12h,过筛,得到Tb<sup>3+</sup>、La<sup>3+</sup>掺杂的Gd<sub>2</sub>O<sub>2</sub>S荧光粉。

### 1.2 实验仪器和测试条件

#### 1.2.1 X射线衍射分析

利用X射线衍射仪(D/max-2500型,日本Rigaku公司)对荧光粉的物相组成与结构进行分析研究。仪器工作条件为:工作电压40kV,工作电流100mA, Ni滤光片,石墨单色器,DS(发散狭缝)1°,SS(防散射狭缝)1°,RS(接收狭缝)0.1mm。波长0.154nm,连续扫描,步径为0.02°,扫描速度8°/min,

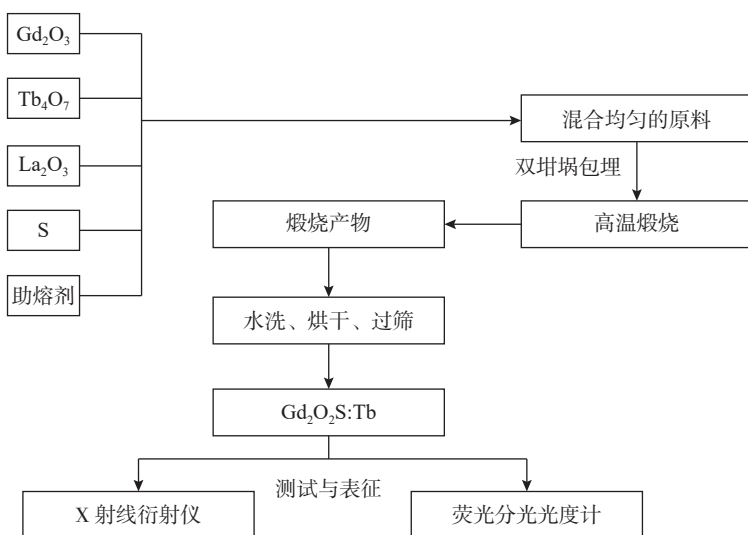


图1 硫熔法制备稀土荧光粉工艺流程

Fig. 1 Process flow for preparing rare earth phosphors by sulfur fusion method.

采用 Cu K $\alpha$  射线,  $2\theta$  角扫描范围为  $10^\circ \sim 80^\circ$ 。

### 1.2.2 光谱性能分析

通过荧光分光光度计 (Lumina 型, 美国 ThermoFisher 公司) 对荧光粉的激发光谱和发射光谱进行分析研究。仪器工作条件为: 激发光谱在 544nm 监测下测得, 发射光谱在 254nm 激发下测得。狭缝宽度 1nm, 探测器电压 500V, 扫面速度 60nm/min。测试过程中为了防止倍频峰的影响, 选用 500nm 的滤光片。波长准确度:  $\pm 0.5\text{nm}$ , 重复性:  $\pm 0.2\text{nm}$ 。

## 2 结果与讨论

### 2.1 Tb<sup>3+</sup>掺杂 Gd<sub>2</sub>O<sub>2</sub>S 荧光粉的物相与发光性能研究

因为 Gd<sub>2</sub>O<sub>2</sub>S 宽敞的六方晶体结构, 能够形成一定数量的阳离子和阴离子空位, 同时可以容纳一定量的间隙离子进入, 而晶体结构并未发生改变。Tb<sup>3+</sup>作为激活剂离子, 它的掺入并没有改变 Gd<sub>2</sub>O<sub>2</sub>S 的六方晶体结构, 但其掺杂浓度对样品的发光性能有着直接的影响。

表1 两种硫氧化物的晶体结构参数比较

Table 1 Comparison of crystal structure parameters of two kinds of oxysulfides.

#### 2.1.1 Tb<sup>3+</sup>掺杂对 Gd<sub>2</sub>O<sub>2</sub>S 荧光粉物相组成的影响

表1 是 Gd<sub>2</sub>O<sub>2</sub>S 与 Tb<sub>2</sub>O<sub>2</sub>S 的晶体参数比较, 可以看出两者的晶体参数以及晶体结构比较接近。图2 为 Tb<sup>3+</sup>掺杂 Gd<sub>2</sub>O<sub>2</sub>S 示意图。由于 Gd<sup>3+</sup>的离子半径为 0.0938nm<sup>[22-23]</sup>, Tb<sup>3+</sup>的离子半径为 0.0923nm, 根据置换型固溶体影响因素<sup>[24]</sup>, 只有当两个组分的晶体结构完全一样且离子电价相等时, 才会形成连续置换型固溶体。当两个离子的离子半径差小于 15% 时, 容易形成连续置换型固溶体; 当大于 15% 小于 30% 时, 会形成有限置换固溶体; 当大于 30% 时, 很难形成固溶体。此外, 当两组分的电负性相差较大则易形成化合物, 而电负性相近的两组分则更有利形成固溶体。表1 中可以看出, Tb<sup>3+</sup>和 Gd<sup>3+</sup>两者的离子半径相近, 带电电荷也相同, 所以 Tb<sup>3+</sup>很容易替代 Gd<sup>3+</sup>进入 Gd<sub>2</sub>O<sub>2</sub>S 的晶格位置, 取代 Gd<sup>3+</sup>形成固溶体。

对不同 Tb<sup>3+</sup>掺杂浓度下 (0.25mol%、0.75mol%、1mol%、2mol%、3mol%、4mol%) 的荧光粉进行 X 射线衍射分析。从图3 中可以看出, 所有样品的衍射峰位置均与标准卡片 JCPDS(No.26-1422) 完全

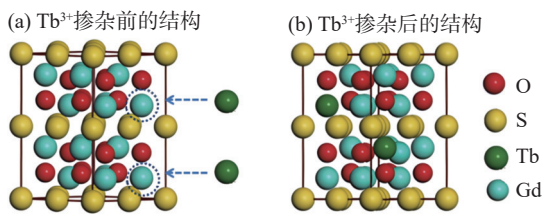
图2  $\text{Tb}^{3+}$ 掺杂  $\text{Gd}_2\text{O}_2\text{S}$ 示意图

Fig. 2 Schematic diagrams of  $\text{Tb}^{3+}$  doped  $\text{Gd}_2\text{O}_2\text{S}$ : (a) Structure before  $\text{Tb}^{3+}$  doping; (b) Structure after  $\text{Tb}^{3+}$  doping.

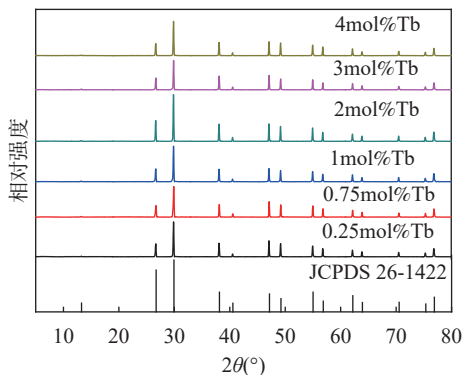
图3 不同  $\text{Tb}^{3+}$ 掺杂浓度下  $(\text{Gd}_{1-x}\text{Tb}_x)_2\text{O}_2\text{S}$  荧光粉的 X 射线衍射图 ( $x=0.25\text{mol}\%$ ,  $0.75\text{mol}\%$ ,  $1\text{mol}\%$ ,  $2\text{mol}\%$ ,  $3\text{mol}\%$ ,  $4\text{mol}\%$ )

Fig. 3 XRD patterns of  $(\text{Gd}_{1-x}\text{Tb}_x)_2\text{O}_2\text{S}$  phosphors at different  $\text{Tb}^{3+}$  doping concentrations ( $x=0.25\text{mol}\%$ ,  $0.75\text{mol}\%$ ,  $1\text{mol}\%$ ,  $2\text{mol}\%$ ,  $3\text{mol}\%$ ,  $4\text{mol}\%$ ).

一致<sup>[13]</sup>, 没有其他的杂质峰, 说明样品中  $\text{Tb}^{3+}$ 已完全掺入到基体的晶格中, 且  $\text{Tb}^{3+}$ 的掺入并没有改变  $\text{Gd}_2\text{O}_2\text{S}$  的六方晶体结构。

### 2.1.2 $\text{Tb}^{3+}$ 掺杂对 $\text{Gd}_2\text{O}_2\text{S}$ 荧光粉发光性能的影响

$\text{Tb}^{3+}$ 的掺杂浓度会直接影响荧光粉的发光强度。通常情况下,  $\text{Tb}^{3+}$ 浓度的提高会增强基质中荧光物质的光发射能力<sup>[25-26]</sup>。这是因为  $\text{Tb}^{3+}$ 离子间的距离缩短能强化它们的自敏化作用, 使得蓝光发射强度减弱的同时绿光发射强度增强。然而, 一旦掺入超过猝灭临界浓度的  $\text{Tb}^{3+}$ ,  $\text{Tb}^{3+}$ 发生了浓度猝灭效应, 自身的“凝聚”和“共振”的现象会导致非辐射跳跃率的上升, 反过来又会降低荧光粉的光发射强度<sup>[27]</sup>。

图4是利用荧光光谱仪对合成的系列  $\text{Tb}^{3+}$ 掺杂的  $\text{Gd}_2\text{O}_2\text{S}$  荧光粉在 254nm 近紫外光激发下的发射光谱图。通过观察光谱图可知, 尽管  $\text{Tb}^{3+}$ 含量有所变化, 但并未对荧光粉的特征发射峰位置产生显著影响。最强的特征发射峰对应的是  $\text{Tb}^{3+}$ 的  $^5\text{D}_4 \rightarrow ^7\text{F}_5$  跃迁, 位于 544nm(绿光区); 此外在 586nm(黄光区)

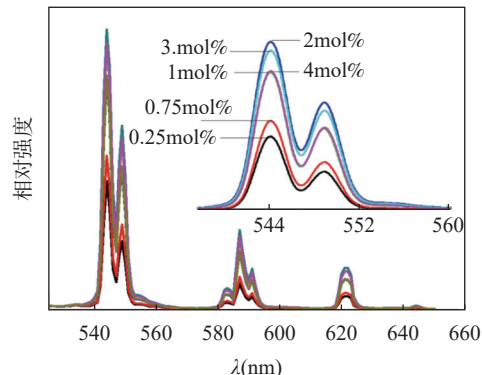
图4 不同  $\text{Tb}^{3+}$ 掺杂浓度下  $(\text{Gd}_{1-x}\text{Tb}_x)_2\text{O}_2\text{S}$  荧光粉的发射光谱 ( $\lambda_{\text{ex}}=254\text{nm}$ ) 谱图 ( $x=0.25\text{mol}\%$ ,  $0.75\text{mol}\%$ ,  $1\text{mol}\%$ ,  $2\text{mol}\%$ ,  $3\text{mol}\%$ ,  $4\text{mol}\%$ )

Fig. 4 The emission spectra of  $(\text{Gd}_{1-x}\text{Tb}_x)_2\text{O}_2\text{S}$  phosphors at various  $\text{Tb}^{3+}$  doping concentrations ( $x=0.25\text{mol}\%$ ,  $0.75\text{mol}\%$ ,  $1\text{mol}\%$ ,  $2\text{mol}\%$ ,  $3\text{mol}\%$ ,  $4\text{mol}\%$ ).

观察到特征发射峰对应  $\text{Tb}^{3+}$ 的  $^5\text{D}_4 \rightarrow ^7\text{F}_4$  跃迁, 以及在 622nm(红光区)观察到特征发射峰对应  $\text{Tb}^{3+}$ 的  $^5\text{D}_4 \rightarrow ^7\text{F}_3$  跃迁。随着  $\text{Tb}^{3+}$ 掺入量的提升, 铟掺杂的硫氧化钆荧光粉的发射峰强度也随之增强。直至  $\text{Tb}^{3+}$ 的掺入量为 2mol% 时光发射强度达到峰值。进一步提高  $\text{Tb}^{3+}$ 的掺入量后, 荧光粉的光发射强度却开始降低, 这意味着本研究中  $\text{Tb}^{3+}$ 的猝灭临界值为 2mol%。

### 2.1.3 $\text{Tb}^{3+}$ 在 $\text{Gd}_2\text{O}_2\text{S}$ 荧光粉基体中的浓度猝灭机理

当  $\text{Tb}^{3+}$ 掺杂浓度增加时, 相邻  $\text{Tb}^{3+}$ 之间的距离减小, 激发的  $\text{Tb}^{3+}$ 可以将吸收到的能量传递给紧邻的发光中心离子  $\text{Tb}^{3+}$ , 直至传递到猝灭中心, 使得荧光粉发光强度降低<sup>[28]</sup>。故  $\text{Tb}^{3+}$ 浓度越高, 发生浓度猝灭可能性也就越大。

在  $\text{Tb}^{3+}$ 掺杂  $\text{Gd}_2\text{O}_2\text{S}$  的系列荧光粉中可以用以下公式(1)<sup>[29]</sup>来估算相邻  $\text{Tb}^{3+}$ 间的距离:

$$R_{\text{Tb-Tb}} \approx 2 \times \left[ \frac{3V}{4\pi X_c N} \right]^{1/3} \quad (1)$$

式中:  $V$ 代表单个晶胞体积;  $X_c$ 代表  $\text{Tb}^{3+}$ 掺杂的浓度;  $N$ 则是指单个晶胞中阳离子的占比。 $\text{Tb}^{3+}$ 掺杂的  $\text{Gd}_2\text{O}_2\text{S}$  荧光粉中,  $V$ 值为  $0.0857\text{nm}^3$ ;  $N$ 值为 2;  $X_c$  值为 0.02。

计算得到,  $\text{Tb}^{3+}$ 掺杂量为 2mol% 时, 相邻  $\text{Tb}^{3+}$ 间的距离为 1.6nm。根据 Dexter 电荷转移机理, 离子之间的能量传递机理存在交互作用和电多级相互作用两类。交互作用通常发生在轨道重叠的离子之间, 所以它们距离在  $0.3 \sim 0.4\text{nm}$ <sup>[30]</sup>。而 1.6nm 远

大于 $0.3\sim0.4\text{nm}$ 的范围,所以电多级相互作用引起了能量在 $\text{Tb}^{3+}$ 内部的浓度猝灭。

${}^5\text{D}_4\rightarrow{}^7\text{F}_J$ 转移到不同能级的过程受到相同猝灭浓度以及衰减规律的影响<sup>[31]</sup>,从浓度猝灭曲线的分析中可以推测 $\text{Tb}^{3+}$ 的浓度猝灭机制。根据 Dexter 电荷转移机理,发光强度  $I$  和激活剂浓度  $\alpha$  的关系如式(2)、(3)所示<sup>[32]</sup>。

$$I \propto \alpha^{(1-\frac{s}{d})} \Gamma(1 + \frac{s}{d}) \quad (2)$$

$$\alpha = C \cdot \Gamma\left(1 - \frac{s}{d}\right) \left[ \frac{X_0(1+A)}{\gamma} \right]^{d/s} \quad (3)$$

式中:电多极级数为  $S$ ;试样样本的维数为  $d$ ,由于 $\text{Tb}^{3+}$ 之间的能量传递发生在晶体颗粒的内部,所以  $d$  值为 3;  $\Gamma(1+S/d)$  是  $\Gamma$  函数<sup>[33]</sup>;  $C$  是  $\text{Tb}^{3+}$ 掺杂量。

式(3)中: $A$  和  $X_0$  为常数,  $\gamma$  为敏化剂的固有跃迁概率。因此,可以推导出公式(4):

$$\log\left(\frac{I}{C}\right) = -\frac{s}{d} \times \log\alpha + \log f \quad (4)$$

式(4)中:当  $S$  分别等于 6、8、10 时,代表了电偶极跃迁相互作用、电偶极-电四级相互作用以及电四级跃迁相互作用。

将  $\text{Tb}^{3+}$  在  $254\text{nm}$  激发下的绿光发射的  ${}^5\text{D}_4\rightarrow{}^7\text{F}_5(544\text{nm})$  跃迁发射强度与  $\text{Tb}^{3+}$  的掺杂量的  $\log(I/x)$  和  $\log(x)$  进行线性拟合,得到结果如图 5 所示。

拟合后得到斜率  $-S/3=-1.966$ ,即  $S \approx 6$ ,故在本研究中  $\text{Tb}^{3+}$ 发生浓度猝灭的主要原因是电偶极跃迁相互作用引起的<sup>[27]</sup>。因此,当  $\text{Gd}_2\text{O}_2\text{S}$  基质中相邻  $\text{Tb}^{3+}$  之间的距离小于  $1.6\text{nm}$  的临界猝灭距离时,电偶极跃迁相互作用,使得  $\text{Tb}^{3+}$  在  ${}^5\text{D}_4$  能级上的数量减少,减弱了荧光粉的光发射强度。

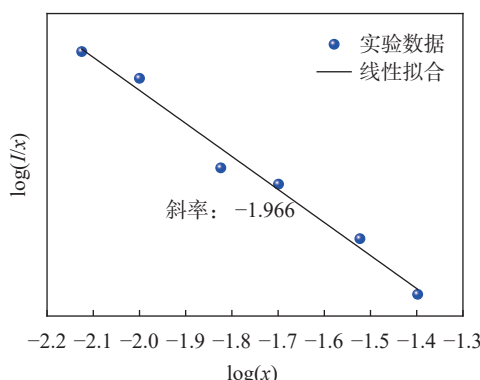


图5  $\text{Tb}^{3+}$  的  ${}^5\text{D}_4\rightarrow{}^7\text{F}_5$  跃迁发射强度  $I$  与掺杂量  $x$  的  $\log(I/x)-\log(x)$  关系

Fig. 5 Relational curves of  $\log(I/x)-\log(x)$  between emission intensity  $I$  of  $\text{Tb}^{3+}$   ${}^5\text{D}_4\rightarrow{}^7\text{F}_5$  and doping concentration  $x$ .

## 2.2 稀土 $\text{La}^{3+}$ 掺杂对荧光粉晶格场及发光性能的影响

按照洪特定律,当离子电子结构的最外层达到全满、半满或者完全空时,其离子稳定性较高。 $\text{La}^{3+}$ 从基态到激发态需要很大的能量,并且在  $200\sim1000\text{nm}$  没有特征发射峰,因此不会对发光中心离子的色纯度有影响,且  $\text{La}^{3+}$ 与  $\text{Gd}^{3+}$ 具有相同的  $\text{P}3\text{ml}$  空间群,所以  $\text{La}^{3+}$ 取代  $\text{Gd}^{3+}$ 后,晶体结构依然保持六方晶相。

### 2.2.1 $\text{La}^{3+}$ 掺杂对荧光粉物相组成的影响

图 6 是不同  $\text{La}^{3+}$ 掺杂浓度 ( $15\text{mol\%}$ 、 $30\text{mol\%}$ 、 $45\text{mol\%}$ 、 $60\text{mol\%}$ ) 的荧光粉的 X 射线衍射谱图,当  $\text{La}^{3+}$ 掺杂量增加后,样品依然保持着纯粹的六方晶体结构。进一步观察 X 射线衍射谱图的细节部分,可以清楚地观察到峰的位置朝较低的角度发生偏移,同时相应的晶体尺寸也在增大。这是由于  $\text{La}^{3+}$ 的半径比  $\text{Gd}^{3+}$ 更大,因此引入  $\text{La}^{3+}$ 会导致晶格扩大,从而使晶胞参数也随之增大。

表 2 是根据德拜-谢乐公式计算的系列  $\text{La}^{3+}$ 掺杂荧光粉的晶粒尺寸,可以观察到随着  $\text{La}^{3+}$ 掺杂浓

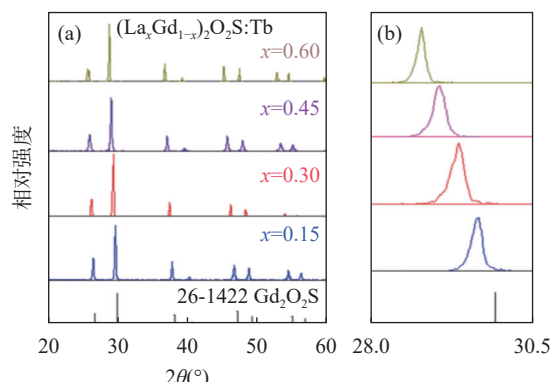


图6  $(\text{La}_x\text{Gd}_{1-x})_2\text{O}_2\text{S}: \text{Tb}$  的 X 射线衍射谱图 ( $x=0.15, 0.30, 0.45, 0.60$ )

Fig. 6 XRD patterns of  $(\text{La}_x\text{Gd}_{1-x})_2\text{O}_2\text{S}: \text{Tb}$  ( $x=0.15, 0.30, 0.45, 0.60$ ).

表2  $(\text{La}_x\text{Gd}_{1-x})_2\text{O}_2\text{S}: \text{Tb}$  的晶粒尺寸 ( $x=0.15, 0.30, 0.45, 0.60$ )

Table 2 Calculated crystalline size of  $(\text{La}_x\text{Gd}_{1-x})_2\text{O}_2\text{S}: \text{Tb}$  phosphor ( $x=0.15, 0.30, 0.45, 0.60$ ).

荧光粉样品	晶粒尺寸 (nm)
$\text{Gd}_2\text{O}_2\text{S}: \text{Tb}$	106.2
$(\text{La}_{0.15}\text{Gd}_{0.85})_2\text{O}_2\text{S}: \text{Tb}$	88.9
$(\text{La}_{0.30}\text{Gd}_{0.70})_2\text{O}_2\text{S}: \text{Tb}$	50.3
$(\text{La}_{0.45}\text{Gd}_{0.55})_2\text{O}_2\text{S}: \text{Tb}$	48.5
$(\text{La}_{0.60}\text{Gd}_{0.40})_2\text{O}_2\text{S}: \text{Tb}$	37.3

度的提高,  $\text{La}^{3+}$ 掺杂荧光粉的晶粒尺寸由最初的从106.2nm逐渐降低至37.3nm。这表明  $\text{La}^{3+}$ 掺杂浓度的提高,会使得晶格发生畸变,从而增加电荷密度。电荷密度的增强又会增强晶粒间的排斥力,限制了晶粒的生长<sup>[34]</sup>。

图7是样品表面电子密度图。从图7b可以看出,晶格表面主要是带有负电荷的硫层,硫层的负电性增大,则排斥力也随之增强。为了更好地了解尺寸变化机理,利用密度泛函理论(DFT)计算了 $\text{Gd}_2\text{O}_2\text{S}$ 、 $(\text{La}_{0.15}\text{Gd}_{0.85})_2\text{O}_2\text{S}$ 和 $(\text{La}_{0.6}\text{Gd}_{0.4})_2\text{O}_2\text{S}$ 的态密度(DOS),以及各个原子的态密度(PDOS)。本研究用Materials Studio软件中的CASTEP模块对稀土 $\text{Tb}^{3+}$ 、 $\text{La}^{3+}$ 掺杂的 $\text{Gd}_2\text{O}_2\text{S}$ 荧光粉的能带结构以及态密度进行计算。因为样品为六方晶体结构,P3ml空间群,晶格常数为: $a=0.3851\text{nm}$ , $b=0.3851\text{nm}$ , $c=0.6664\text{nm}$ , $\alpha=90^\circ$ , $\beta=90^\circ$ , $\gamma=120^\circ$ 。CASTEP(Cambridge sequential total energy package)是基于密度泛函方法(DFT)来进行量子力学的计算<sup>[35]</sup>。研究中选用了广义梯度近似的(GGA),基于DFT的第一性原理平面波超软赝势方法(Utrisoft pseudopotential)来模拟计算<sup>[36]</sup>。计算中,选取了各原子的价电子组态分别为Gd( $4f^75s^25p^65d^16s^2$ )、La( $5s^25p^65d^16s^2$ )、S( $3s^23p^4$ )以及O( $2s^22p^4$ )<sup>[37]</sup>,在倒易k空间中,平面波截断能量 $E_{cut}=360\text{eV}$ ,收敛精度选取 $2\times10^{-6}\text{eV}$ 。用Monkors-Park网格法进行K点选取,K网格大小为 $4\times4\times2$ ,能量计算在倒易空间中进行,通过布里渊区的积分计算荧光粉的电子结构。通过 $E_g=1240/\lambda_g(\text{eV})$ 计算,可以得出三种荧光粉的禁带宽度分别为4.22eV、3.82eV和3.52eV。PDOS的价带顶主要由氧元素的2p轨道以及硫元素的2p轨道组成;导带则由钆元素的5d轨道以及镧元素的5d轨道组成。

从图8中的 $\text{Gd}_2\text{O}_2\text{S}$ 、 $(\text{La}_{0.3}\text{Gd}_{0.7})_2\text{O}_2\text{S}$ 以及 $(\text{La}_{0.6}\text{Gd}_{0.4})_2\text{O}_2\text{S}$ 的能带结构图与态密度图中可以看出,由于 $\text{La}^{3+}$ 掺杂浓度的提高,导带态密度也随之逐渐增

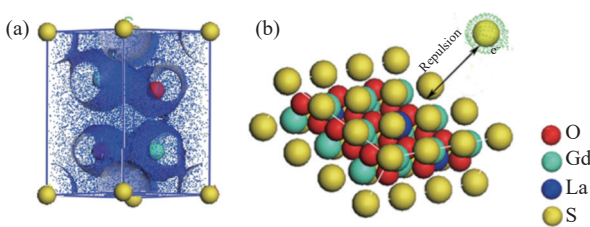


图7 电子密度等面图

Fig. 7 Contour maps of electron density.

大。表面电荷密度又会由于态密度的增大而加强,从而增强了荧光粉晶粒间的排斥力。此外,态密度越强对应的能隙越小,所以导带宽度的增大,导致能隙缩小。

表3则是将 $\text{Gd}_2\text{O}_2\text{S}$ 基体和 $\text{Tb}^{3+}$ 、 $\text{La}^{3+}$ 掺杂的 $\text{Gd}_2\text{O}_2\text{S}$ 荧光粉中各原子对应的价态以及键长进行了对比。用Materials Studio软件进行计算,发现均存在两种金属-氧键(Gd-O)。引入 $\text{La}^{3+}$ 后,荧光粉的键长相较于 $\text{Gd}_2\text{O}_2\text{S}$ 更长, $\text{Gd}_2\text{O}_2\text{S}$ 中原子的价态更高。从掺入稀土离子后硫原子的负电性增强也可证实表面排斥力得到了增强。

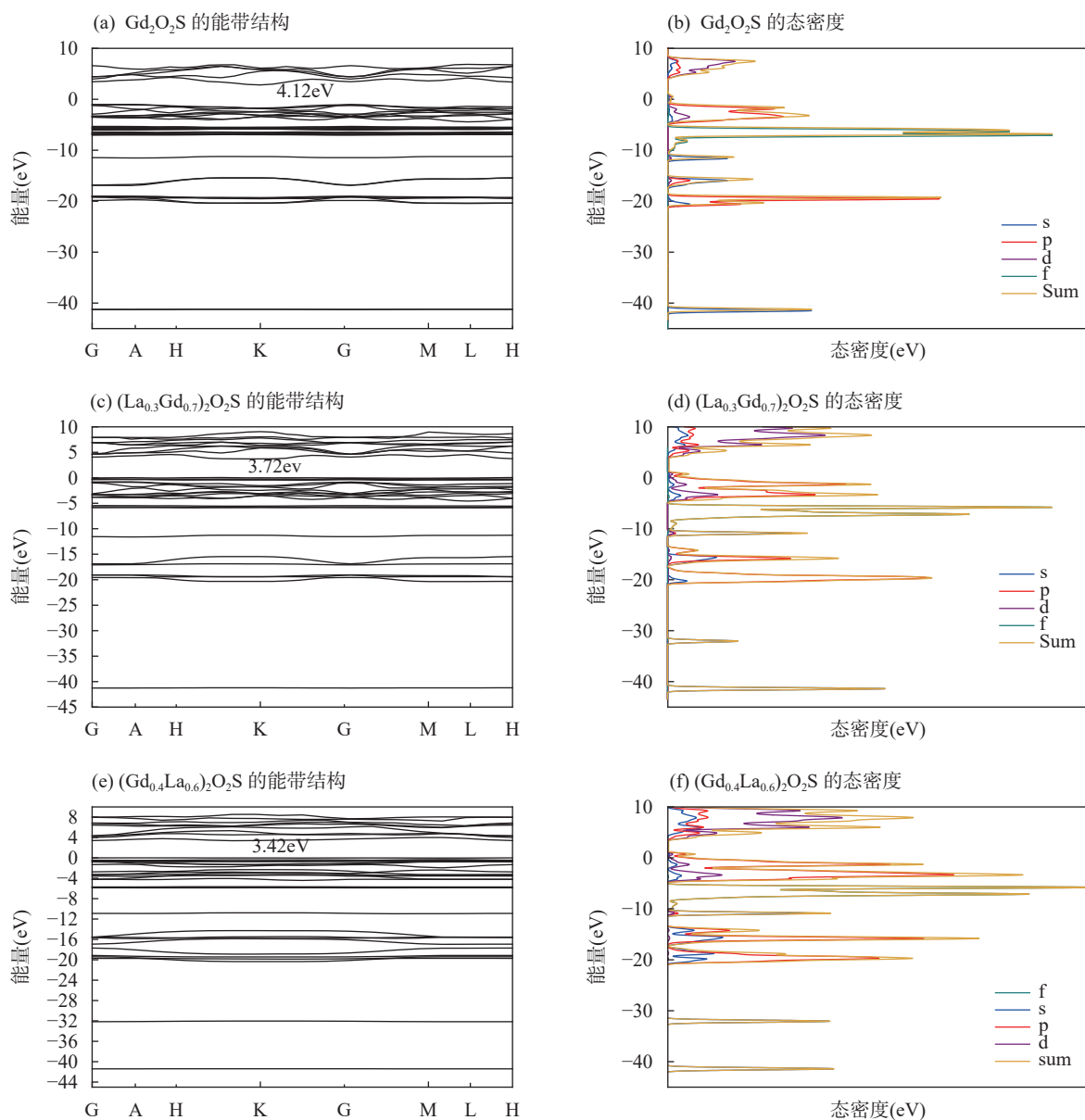
## 2.2.2 $\text{La}^{3+}$ 掺杂对荧光粉发光性能的影响

图9是不同 $\text{La}^{3+}$ 掺杂浓度(0、15mol%、30mol%、45mol%、60mol%)的样品的荧光光谱图。在254nm激发下,稀土掺杂的 $\text{Gd}_2\text{O}_2\text{S}$ 荧光粉的特征发射峰位置没有明显改变,发光强度随着 $\text{La}^{3+}$ 掺杂量的增加而逐渐增强,当 $\text{La}^{3+}$ 掺杂浓度为60mol%时,发光强度为未掺杂 $\text{La}^{3+}$ 时的1.9倍。

图10是不同 $\text{La}^{3+}$ 掺杂浓度(15mol%、30mol%、45mol%、60mol%)的荧光粉在544nm下的激发光谱,并用高斯函数将 $\text{Tb}^{3+}$ 掺杂的 $\text{Gd}_2\text{O}_2\text{S}$ 荧光粉、 $\text{La}^{3+}$ 掺杂量为30mol%的荧光粉以及 $\text{Tb}^{3+}$ 掺杂的 $\text{La}_2\text{O}_2\text{S}$ 荧光粉的激发光谱宽峰进行拟合。其中,绿线为高斯函数曲线,红线为实验曲线,黑线为拟合曲线,方便观察掺杂 $\text{La}^{3+}$ 对荧光粉激发光谱的影响,可以看出,激发光谱随着 $\text{La}^{3+}$ 掺杂量的增加有逐渐蓝移的趋势。随着 $\text{La}^{3+}$ 掺杂量的增加,基质吸收中心( $\text{Gd}^{3+}$ )会逐渐向左移动,从而使得整个基质吸收带左移,故激发光谱发生蓝移。而吸收带的迁移又与晶格场环境有关,对于稀土离子来说,晶格场越强,吸收带越容易往低波段发生迁移<sup>[38]</sup>。结合图8,发现导带宽度的增加,使得原子轨道延展,会增强晶格场。此外,荧光粉的共价性减弱,使得稀土离子的离子性增强,离子间距离缩短,库伦力增大,基质吸收带向低波段移动。由此,随着 $\text{La}^{3+}$ 掺杂量的增加,逐渐增强的晶格场,使得荧光粉的激发光谱蓝移。

## 2.2.3 $\text{La}^{3+}$ 掺杂对荧光粉晶体结构对称性的影响

图11是不同 $\text{La}^{3+}$ 掺杂浓度(0、15mol%、30mol%、45mol%、60mol%)样品在 $\text{Tb}^{3+}$ 544nm发射和254nm激发测得的荧光衰减曲线。Bedekar认为荧光衰减与发光中心离子数目、 $\text{Gd}_2\text{O}_2\text{S}$ 基质中能量迁移以及杂质有关<sup>[39-40]</sup>,且发光中心离子周围的晶格场环境会影响 $\text{Tb}^{3+}$ 的荧光衰减时间<sup>[40]</sup>。荧光粉的衰减时间会随着晶体结构对称性的增强而逐渐



图中 s、p、d、f 分别代表 s、p、d、f 轨道对态密度的贡献。

图8  $\text{Gd}_2\text{O}_2\text{S}$ ,  $(\text{La}_{0.3}\text{Gd}_{0.7})_2\text{O}_2\text{S}$  以及  $(\text{La}_{0.6}\text{Gd}_{0.4})_2\text{O}_2\text{S}$  的能带结构图、态密度图

Fig. 8 The band structure diagrams and density of states diagrams of  $\text{Gd}_2\text{O}_2\text{S}$ ,  $(\text{La}_{0.3}\text{Gd}_{0.7})_2\text{O}_2\text{S}$  and  $(\text{La}_{0.6}\text{Gd}_{0.4})_2\text{O}_2\text{S}$  (s, p, d, and f represent the contributions of s, p, d, and f orbitals to the density of states, respectively).

表3  $\text{Tb}^{3+}$ 掺杂的  $\text{Gd}_2\text{O}_2\text{S}$  荧光粉以及  $(\text{La}_{0.3}\text{Gd}_{0.7})_2\text{O}_2\text{S}$  的键长和各原子对应的价态

Table 3 Bond length and charge of atoms of  $\text{Gd}_2\text{O}_2\text{S}:\text{Tb}$  and  $(\text{La}_{0.3}\text{Gd}_{0.7})_2\text{O}_2\text{S}$ .

样品	键长(nm)			价态		
	Gd-O <sub>1</sub>	Gd-O <sub>2</sub>	Gd-S	Gd	S	O
$\text{Gd}_2\text{O}_2\text{S}$	0.2263	0.2704	0.2859	0.95	-0.53	-0.69
$(\text{Gd}_{0.7}\text{La}_{0.3})_2\text{O}_2\text{S}$	0.2283	0.2533	0.2923	0.81	-0.56	-0.67/-0.79

增长<sup>[41]</sup>。

荧光粉的衰减曲线需符合式(5)双指数衰减公

式<sup>[42]</sup>。式中  $I$  是  $t$  时间的光强;  $A$ 、 $B_1$ 、 $B_2$  都是常数;

而  $\tau_1$  和  $\tau_2$  则代表了两个不同的时间常数, 分别对应

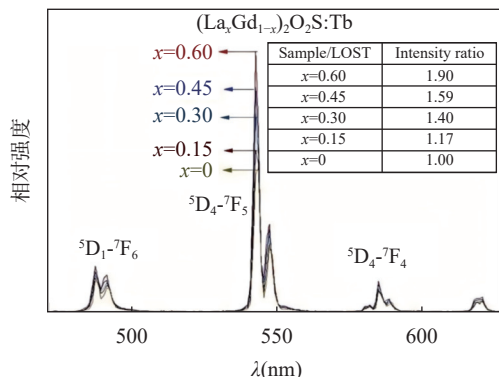
图9 254nm 激发下  $(\text{Gd}_{1-x}\text{La}_x)_2\text{O}_2\text{S:Tb}$  的发射光谱

Fig. 9 Phosphor emission spectra of  $(\text{Gd}_{1-x}\text{La}_x)_2\text{O}_2\text{S:Tb}$  excited by 254nm.

于两个发光中心:

$$I(\tau) = A + B_1 \exp(-t/\tau_1) + B_2 \exp(-t/\tau_2) \quad (5)$$

由式(6)可以计算出荧光粉的平均荧光寿命<sup>[43]</sup>:

$$\tau_{\text{avg}} = \frac{B_1 \tau_1^2 + B_2 \tau_2^2}{B_1 \tau_1 + B_2 \tau_2} \quad (6)$$

当不掺杂  $\text{La}^{3+}$  以及  $\text{La}^{3+}$  的掺杂量为 15mol%、30mol%、45mol%、60mol% 时, 荧光寿命分别对应 565μs、905μs、672μs、612μs 以及 589μs。当  $\text{Tb}^{3+}$  掺

杂的  $\text{Gd}_2\text{O}_2\text{S}$  荧光粉引入  $\text{La}^{3+}$  后,  $\text{La}^{3+}$  会破坏晶体原有的对称性, 从而产生了晶格缺陷。但也正是由于晶格缺陷的出现, 使得荧光粉的荧光寿命得到增长。当  $\text{La}^{3+}$  的掺杂量为 15mol% 时, 荧光寿命从  $\text{Gd}_2\text{O}_2\text{S}$  基体的 565μs 增至 905μs。但对于发光中心离子  $\text{Tb}^{3+}$ ,  $\text{La}^{3+}$  掺杂量增加会使  $\text{Tb}^{3+}$  周围晶格场环境的不对称性增强, 所以当  $\text{La}^{3+}$  的掺杂量从 15mol% 逐渐增加至 60mol% 时, 可以发现荧光粉的荧光寿命又逐渐降低, 这也与图9发光规律一致。因此, 在  $\text{Tb}^{3+}$  掺杂的  $\text{Gd}_2\text{O}_2\text{S}$  荧光粉中, 随着  $\text{La}^{3+}$  掺杂量的增加, 晶格场的对称性逐渐降低, 光发射强度逐渐增强。

### 3 结论

利用 X 射线衍射仪、荧光分光光度计等测试表征手段, 对掺杂稀土离子  $\text{Tb}^{3+}$ 、 $\text{La}^{3+}$  的  $\text{Gd}_2\text{O}_2\text{S}$  荧光粉的相组成、光谱特性进行了研究, 并对其中的“浓度猝灭机理”, “晶格场对称性”进行了初步探讨。结果表明,  $\text{Tb}^{3+}$  的掺杂量对荧光粉的发光性能有显著影响, 当  $\text{Tb}^{3+}$  掺杂量为 2mol% 时,  $\text{Tb}^{3+}$  掺杂的  $\text{Gd}_2\text{O}_2\text{S}$  荧光粉光发射强度最大; 当  $\text{Tb}^{3+}$  掺杂量大于 2mol% 时, 发生了电偶极相互作用引起的浓度猝灭

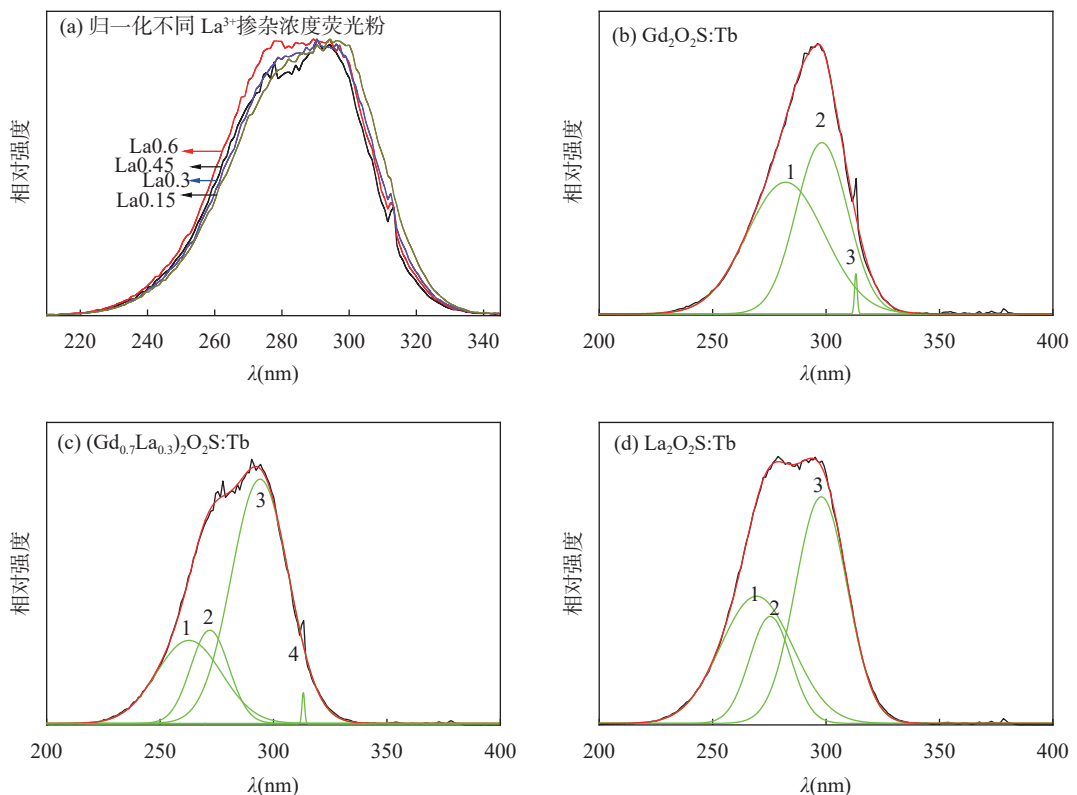
图10  $(\text{Gd}_{1-x}\text{La}_x)_2\text{O}_2\text{S:Tb}$  的激发谱 (544nm)

Fig. 10 Excitation spectra of  $(\text{Gd}_{1-x}\text{La}_x)_2\text{O}_2\text{S:Tb}$  phosphors monitored at 544nm.

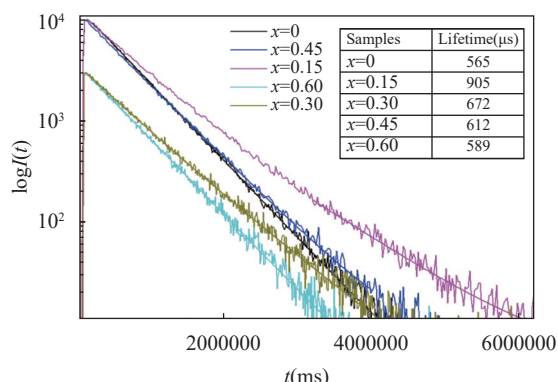


图11  $(\text{La}_x\text{Gd}_{1-x})_2\text{O}_2\text{S:Tb}$  荧光衰减曲线 ( $x=0, 0.15, 0.30, 0.45, 0.6$ )

Fig. 11 Fluorescence attenuation curves of  $(\text{La}_x\text{Gd}_{1-x})_2\text{O}_2\text{S:Tb}$  ( $x=0, 0.15, 0.30, 0.45, 0.6$ ).

现象, 相邻的发光中心离子之间的临界猝灭距离为1.6nm。引入掺杂离子  $\text{La}^{3+}$ 会增加硫层的电负性, 晶格发生畸变, 增强晶粒间的排斥力, 限制了晶粒的生长。随着  $\text{La}^{3+}$ 掺杂量的提高, 荧光粉的晶格场增强,  $\text{Tb}^{3+}$ 周围环境的不对称性增强, 激发光谱向低角度移动, 光发射强度得到增强。

采用硫熔法制备稀土  $\text{Tb}^{3+}$ 、 $\text{La}^{3+}$ 掺杂的  $\text{Gd}_2\text{O}_2\text{S}$  荧光粉, 有效地提高了荧光粉的光发射强度, 为进一步制备粒径分布均匀、色纯度高、光发射强度大的荧光粉奠定了基础。今后利用水热法和硫熔法联合的方式来控制颗粒的形貌以及粒径大小, 有望得到发光更均匀的荧光粉。

## Influence of Rare Earth Terbium and Lanthanum Doping on the Lattice Field and Luminescence Performance of Gadolinium Oxysulfide

ZHANG Jing<sup>1,2</sup>, XU Naicen<sup>1</sup>, SHEN Jialin<sup>1\*</sup>, JIN Fan<sup>1</sup>

(1. Nanjing Center, China Geological Survey, Nanjing 210016, China;

2. Nanjing Tech University, Nanjing 211816, China)

### HIGHLIGHTS

- (1)  $\text{Tb}^{3+}$  doped  $\text{Gd}_2\text{O}_2\text{S}$  phosphors were prepared via the sulfur-melting method, and the impact of  $\text{Tb}^{3+}$  doping concentration on the fluorescence properties of  $\text{Gd}_2\text{O}_2\text{S}$  was studied.
- (2) The rare earth ion  $\text{La}^{3+}$  was introduced to substitute the matrix ion  $\text{Gd}^{3+}$  in  $\text{Gd}_2\text{O}_2\text{S}$ , altering the crystal field environment surrounding  $\text{Tb}^{3+}$ , and effectively improving the fluorescence properties of  $\text{Gd}_2\text{O}_2\text{S}$ .
- (3) The energy transfer mechanisms of  $\text{Tb}^{3+}$  and  $\text{La}^{3+}$  within the  $\text{Gd}_2\text{O}_2\text{S}$  matrix were explored, and the mechanism of action of rare earth ion doping on the  $\text{Gd}_2\text{O}_2\text{S}$  phosphor was analyzed.

**ABSTRACT:** Rare earth oxysulfides possess excellent energy transfer efficiency, along with remarkable thermal and chemical stabilities. Currently, it remains a challenging research focus to fluorescent powder characterized by a small particle size, narrow distribution, and high luminescence intensity. Here, we primarily investigate ways to enhance the luminescent intensity of rare earth sulfur oxide phosphors synthesized via the sulfur fusion method and to reduce the particle size of these phosphors. By using the sulfur melting technique, fluorescent powder was created, with doping ions  $\text{Tb}^{3+}$  and  $\text{La}^{3+}$  of rare earth integrated. Various methods such as fluorescence spectroscopy, and X-ray diffraction were employed to investigate how rare earth terbium and lanthanum doping impacts the lattice structure and luminescent capabilities of gadolinium oxysulfide. The experimental results indicate that the fluorescent powder has a pure hexagonal crystal structure. The luminescence intensity of the fluorescent powder reaches its maximum when the doping concentration of  $\text{Tb}^{3+}$  is 2mol%. When the  $\text{La}^{3+}$  doping concentration is 60mol%, the luminescence intensity is 1.9 times that of the undoped  $\text{La}^{3+}$  sample. Therefore, introducing rare earth terbium and lanthanum atoms can effectively improve the optical properties of fluorescent powders. The BRIEF REPORT is available for this paper at <http://www.ykcs.ac.cn/en/article/doi/10.15898/j.ykcs.202405070105>.

**KEY WORDS:** luminescence; rare-earth doping; gadolinium oxysulfide; fluorescence spectrophotometry; X-ray diffraction

## BRIEF REPORT

**Significance:** Luminescent material made of rare earth sulfur oxides has garnered significant attention due to its excellent light absorption and transmission properties<sup>[10-12]</sup>, and has been successfully applied in various fields such as optoelectronic devices, magnetic materials, catalysts, etc<sup>[13-15]</sup>.

Researchers have recently conducted a comprehensive investigation into the physical and chemical properties of rare earth sulfur oxides, as well as their preparation methods, revealing that the particle morphology, size, and the ratio of raw materials are all significant factors. Meanwhile, the luminescent properties of rare earth sulfur oxides are influenced by the heat treatment temperature and flux selection<sup>[17-18]</sup>. Qian et al<sup>[19]</sup> synthesized Gd<sub>2</sub>O<sub>2</sub>S phosphors doped with Tb<sup>3+</sup> and Sm<sup>3+</sup> by the hydrothermal method. The resulting phosphor exhibits a capsule-like morphology and a hexagonal crystal structure, coupled with excellent luminescent properties. By changing the ion concentration and the excitation wavelength, adjustable luminescence of various colors from green light to orange red light can be achieved. By changing the dopant ion concentration and the excitation wavelength, tunable luminescence of various colors from green light to orange red light can be achieved. Jiang et al<sup>[20]</sup> synthesized Tb<sup>3+</sup> doped Gd<sub>2</sub>O<sub>2</sub>S phosphors in various morphologies, including flakes, spheres, squares, prisms, and rods by adjusting the pH value of the solution. The findings reveal that all these phosphor forms possess a pure hexagonal phase. As the shape varies, the band gap energy of the phosphor gradually increases from 3.76eV to 4.28eV, and the luminescence performance adjusts accordingly. Notably, phosphors with spherical and cubic microstructures exhibit superior luminescent properties, and the emission color of the resulting phosphors is significantly affected by the excitation source. Machado et al<sup>[21]</sup> investigated the synthesis of a series of Er<sup>3+</sup> doped Gd<sub>2</sub>O<sub>2</sub>S phosphors and Er<sup>3+</sup> and Yb<sup>3+</sup> doped Gd<sub>2</sub>O<sub>2</sub>S phosphors using the rapid microwave-assisted solid-phase method (MASS). Two distinct precursor compounds were employed, rare earth oxide (Ln<sub>2</sub>O<sub>3</sub>) and hydroxycarbonate [Ln(OH)CO<sub>3</sub>], with Ln representing Gd, Er, and Yb. The findings indicate that substituting Ln(OH)CO<sub>3</sub> for the conventional Ln<sub>2</sub>O<sub>3</sub> in MASS synthesis facilitates a uniform distribution of Er<sup>3+</sup> and Yb<sup>3+</sup> within the Gd<sub>2</sub>O<sub>2</sub>S matrix, resulting in enhanced up-conversion luminescence properties. Moreover, the MASS method reduces preparation time by 79% and energy consumption by 93% compared to traditional solid-phase techniques. The sulfur melting method, being the most widely adopted approach, is characterized by its operational simplicity and the outstanding luminescence performance of the resulting powder. However, samples synthesized through this method are highly prone to agglomeration, typically resulting in a relatively large particle size. For phosphors, having a regular geometric shape and smaller particle size can enhance the bulk density of the particles. This, in turn, reduces the energy scattering rate, enabling the generation of more uniform light emission. Simultaneously, as the particle size decreases, the specific surface area increases. A larger specific surface area often leads to the presence of a significant number of surface defects. These defects, conversely, can cause a decline in the luminous intensity. Consequently, the acquisition of gadolinium oxysulfide fluorescent powder, which is characterized by a small particle size, a narrow distribution, and high luminescence intensity, remains a challenging research focus.

To optimize the luminescence intensity and resolution of fluorescent powder synthesized by the sulfur melting method, a systematic study was conducted. First, the effect of Tb<sup>3+</sup> doping on the fluorescent powder's characteristics was carefully examined. Then, the impacts of introducing the rare earth modifying ion La<sup>3+</sup> on the powder's structural and physicochemical properties were elucidated. Characterization methods such as X-ray diffractometry and fluorescence spectrophotometry were used. The "concentration quenching mechanism" and "lattice field symmetry" were preliminarily explored. Research has revealed that the luminescence intensity attains

its maximum value when the  $\text{Tb}^{3+}$  doping concentration is 2mol%. When the  $\text{La}^{3+}$  doping concentration reaches 60mol%, the luminescence intensity is 1.9 times that of the sample without  $\text{La}^{3+}$  doping, indicating a significant enhancement in luminescence. This sulfur melting method has effectively improved the light emitting intensity of the phosphors. Consequently, it has established a robust basis for the subsequent fabrication of phosphors that feature a uniform particle size distribution, high color purity, and high light emitting intensity.

**Methods:** In this study, we precisely measured gadolinium oxide, sublimated sulfur, anhydrous sodium carbonate, terbium oxide, and lanthanum oxide in accordance with the stoichiometric ratio. The material was mixed with the agate balls and placed on a ball mill for 10h to ensure thorough and even mixing. After the mixed material was dried, it was subjected to calcination in a high-temperature programmed furnace using a double crucible embedding method. The heat treatment temperature was set to heat from room temperature to 270°C and maintained for 1h, followed by an increase to 1100°C for 3h, with a heating rate of 5°C/min. The calcined powder was cooled naturally, placed in a beaker, washed three times with deionized water and then suction filtered. After undergoing repeated washing and suction filtration three times, the sample was placed in a drying oven and dried at 80°C for 12h. Subsequently,  $\text{Tb}^{3+}$  and  $\text{La}^{3+}$  doped  $\text{Gd}_2\text{O}_2\text{S}$  phosphor was obtained through sieving.

Utilizing the Rigaku Corporation's D/max-2500 X-ray diffractometer, we conducted an assessment of the sample's phase composition and structure. The operating conditions were as follows: working voltage 40kV, working current 100mA, Ni filter, graphite monochromator, DS (diverging slit) 1°, SS (anti scattering slit) 1°, RS (receiving slit) 0.1mm. The optimum wavelength is 0.154nm, continuous scanning, step size of 0.02°, scanning speed of 8°/min, using Cu K $\alpha$  rays, with a 2 $\theta$  angle scanning range of 10°–80°. A fluorescence spectrophotometer (Lumina, ThermoFisher Scientific, USA) was utilized to evaluate the excitation and emission spectra of the sample. The excitation spectrum was measured under 544nm monitoring, and the emission spectrum was measured under 254nm excitation. The slit width was set to 1nm, the detector voltage to 500V, and the scanning speed to 60nm/min. To avoid the impact of doubling peaks during the testing process, a 500nm filter was chosen. Wavelength accuracy was  $\leq 0.5\text{nm}$ , and repeatability was  $\leq 0.2\text{nm}$ .

**Data and Results:** The phosphor's luminescence intensity is significantly influenced by the doping concentration of  $\text{Tb}^{3+}$ . When the  $\text{Tb}^{3+}$  concentration ranges from 0.25mol% to 4mol%, the luminescence intensity at 544nm initially increases and then decreases. Specifically, when the  $\text{Tb}^{3+}$  concentration reaches 2mol%, the luminescence intensity at 544nm peaks. Once the  $\text{Tb}^{3+}$  doping concentration exceeds 2mol%, a concentration quenching phenomenon occurs (Fig.4). This phenomenon can be ascribed to electric dipole-dipole interactions. According to Dexter's theory, the concentration quenching of the  $^5\text{D}_4 \rightarrow ^7\text{F}_5$  transition of  $\text{Tb}^{3+}$  is caused by the dipole-dipole effect, and the quenching distance is approximately 1.6nm. Moreover, the incorporation of  $\text{La}^{3+}$  doping ions enhanced the electronegativity of the sulfur layer, consequently inducing lattice distortion. As the amount of  $\text{Gd}^{3+}$  replaced by  $\text{La}^{3+}$  increased, the XRD peaks shifted towards lower diffraction angles (Fig.6), and the corresponding unit cell parameters gradually expanded. According to density functional theory (DFT) and Mott-David theory, calculations revealed that the band gap of  $(\text{Gd}_{1-x}\text{La}_x)_2\text{O}_2\text{S}:\text{Tb}$  decreases as the  $\text{La}^{3+}$  concentration rises and the valence states change (Fig.8). Notably, the increasing electronegativity of S strengthens the repulsive force on the crystal surface. When the  $\text{La}^{3+}$  concentration ranges from 15mol% to 60mol%, the excitation spectra shift towards shorter wavelengths. This shift enhances the luminescence intensity of the  $\text{Gd}_2\text{O}_2\text{S}$  phosphors co-doped with rare earth  $\text{Tb}^{3+}$  and  $\text{La}^{3+}$ . Under 254nm excitation, the luminescence intensity of the emission spectrum gradually increases (Fig.9). Measurement of the phosphors' decay time showed that the symmetry of the crystals progressively decreases with the increase in  $\text{La}^{3+}$  doping concentration (Fig.11).

## 参考文献

- [1] Maharram J, Kelly E C, Cameron L R, et al. Impact of structural changes on energy transfer in the anion-engineered  $\text{Re}^{3+}$ :  $\text{Y}_2\text{O}_3$  through low-temperature synthesis approach[J]. *The Journal of Physical Chemistry C*, 2024, 128(6): 2625–2633.
- [2] Ma Y, Lu W, Xu Z L, et al.  $\text{RE}_2\text{O}_2\text{S}: \text{Tb}^{3+}$  ( $\text{RE}=\text{Y}, \text{La}, \text{Gd}$ ): Comparable research on morphology, luminescence, thermal stability and magnetic property[J]. *Ceramics International*, 2023, 49(9): 14367–14376.
- [3] Qian B F, Wang Z, Wang Y L, et al. Comparative study on the morphology, growth mechanism and luminescence property of  $\text{RE}_2\text{O}_2\text{S}: \text{Eu}^{3+}$  ( $\text{RE} = \text{Lu}, \text{Gd}, \text{Y}$ ) phosphors[J]. *Journal of Alloys and Compounds*, 2021, 870: 159273.
- [4] 韩萧萧, 梁涛, 王思雨, 等. 电感耦合等离子体质谱联用技术在稀土元素物源指示研究中的应用进展[J]. *岩矿测试*, 2023, 42(1): 1–15.  
Han X X, Liang T, Wang S Y, et al. A review of research progress on provenance indication of rare earth elements by inductively coupled plasma-mass spectrometry hyphenated techniques[J]. *Rock and Mineral Analysis*, 2023, 42(1): 1–15.
- [5] 黄海波, 袁静, 凌波, 等. 电弧发射光谱技术发展及其在地质领域的应用[J]. *华东地质*, 2023, 44(1): 103–117.  
Huang H B, Yuan J, Ling B, et al. Technical development of arc-emission spectroscopy and its application in geological sample analysis[J]. *East China Geology*, 2023, 44(1): 103–117.
- [6] Luo X X, Cao W H. Ethanol-assistant solution combustion method to prepare  $\text{La}_2\text{O}_2\text{S}: \text{Yb}, \text{Pr}$  nanometer phosphor[J]. *Journal of Alloys and Compounds*, 2008, 460: 529–534.
- [7] 李欣尉, 李超, 周利敏, 等. 富碳质地质样品 Re-Os 同位素体系研究进展[J]. *岩矿测试*, 2023, 42(2): 221–238.  
Li X W, Li C, Zhou L M, et al. A review of research progress on Re-Os isotopic system of carbon-enriched geological samples[J]. *Rock and Mineral Analysis*, 2023, 42(2): 221–238.
- [8] 许少鸿. 固体发光[M]. 北京: 清华大学出版社, 2011.  
Xu S H. Luminescence of solid[M]. Beijing: Tsinghua University Press, 2011.
- [9] 朱凡, 由芳田, 时秋峰, 等.  $\text{GdBO}_3: \text{Pr}^{3+}, \text{Yb}^{3+}$  中  $\text{Pr}^{3+}$  到  $\text{Yb}^{3+}$  的能量传递及发光性质[J]. *发光学报*, 2015(7): 751–756.  
Zhu F, You F T, Shi Q F, et al. Luminescence properties and energy transfer from  $\text{Pr}^{3+}$  to  $\text{Yb}^{3+}$  in  $\text{GdBO}_3: \text{Pr}^{3+}, \text{Yb}^{3+}$ [J]. *Chinese Journal of Luminescence*, 2015(7): 751–756.
- [10] Zhang L, Dong L P, Xu Y H, et al. Site occupancy preference of  $\text{Bi}^{3+}$  and  $\text{Bi}^{3+}\text{-Eu}^{3+}$  codoped yttrium gallate phosphors for white LEDs[J]. *Dalton Transactions*, 2021, 50(4): 1366–1373.
- [11] 赵文志, 谢旭, 张兵兵, 等. 深共晶溶剂在生态地质样品分析中的应用研究[J]. *华东地质*, 2024, 45(1): 78–87.  
Zhao W Z, Xie X, Zhang B B, et al. Application of deep eutectic solvent extraction in eco-geological sample analysis[J]. *East China Geology*, 2024, 45(1): 78–87.
- [12] He F Q, Song E H, Chang H, et al. Interstitial  $\text{Li}^+$  occupancy enabling radiative/nonradiative transition control toward highly efficient  $\text{Cr}^{3+}$ -based near-infrared luminescence[J]. *ACS Applied Materials & Interfaces*, 2022, 14(27): 31035–31043.
- [13] 陈江敏, 赖凤琴, 康立强, 等. 溶胶-凝胶法制备  $\text{Gd}_2\text{Zr}_2\text{O}_7: \text{Eu}^{3+}$  红色荧光粉及其发光性能研究[J]. *中国稀土学报*, 2024, 42(4): 666–674.  
Chen J M, Lai F Q, Kang L Q, et al. Preparation and luminescence properties of  $\text{Gd}_2\text{Zr}_2\text{O}_7: \text{Eu}^{3+}$  red phosphor via sol-gel method[J]. *Journal of Rare Earths*, 2024, 42(4): 666–674.
- [14] Xie X L, Xiao P, Pang L, et al. Facile synthesis of yolk-shell  $\text{Si}@\text{void}@C$  nanoparticles with 3D conducting networks as free-standing anodes in lithium-ion batteries[J]. *Journal of Alloys and Compounds*, 2023, 931: 167473.
- [15] 刘晓, 张启燕, 史维鑫, 等. 北羌塘盆地东部上三叠统波里拉组碳酸盐岩矿物特征分析[J]. *岩矿测试*, 2024, 43(3): 440–448.  
Liu X, Zhang Q Y, Shi W X, et al. Mineralogical characteristics of carbonate rocks of the upper Triassic Bolila Formation in the eastern part of the North Qiangtang Basin[J]. *Rock and Mineral Analysis*, 2024, 43(3): 440–448.
- [16] 李江, 丁继扬, 黄新友. 稀土离子掺杂  $\text{Gd}_2\text{O}_2\text{S}$  闪烁陶瓷的研究进展[J]. *无机材料学报*, 2021, 36(8): — 265 —

- 789–806.
- Li J, Ding J Y, Huang X Y. Rare earth doped  $\text{Gd}_2\text{O}_2\text{S}$  scintillation ceramics[J]. *Journal of Inorganic Materials*, 2021, 36(8): 789–806.
- [17] 温汉捷, 周正兵, 马万平, 等. 黑色岩系型战略性关键矿产资源研究进展及主要科学问题[J]. *矿物岩石地球化学通报*, 2024, 43(1): 14–34.  
Wen H J, Zhou Z B, Ma W P, et al. Research progresses and main scientific issues of strategically critical minerals in black rock series[J]. *Bulletin of Mineralogy, Petrology and Geochemistry*, 2024, 43(1): 14–34.
- [18] 黄学勇, 高茂生, 侯国华, 等. 莱州湾海洋沉积物粒度特征及其环境响应分析[J]. *华东地质*, 2023, 44(4): 402–414.  
Huang X Y, Gao M S, Hou G H, et al. Grain size characteristics and environmental response of marine sediments in Laizhou Bay[J]. *East China Geology*, 2023, 44(4): 402–414.
- [19] Qian B F, Wang Y L, Zhao Q R, et al. Adjustable multi-color luminescence and energy transfer of capsule-shaped  $\text{Gd}_2\text{O}_2\text{S}: \text{Tb}^{3+}, \text{Sm}^{3+}$  phosphors[J]. *Journal of Luminescence*, 2022, 244: 118715.
- [20] Jiang P, Li Z P, Lu W, et al. The pH value control of morphology and luminescence properties of  $\text{Gd}_2\text{O}_2\text{S}: \text{Tb}^{3+}$  phosphors[J]. *Materials*, 2022, 15(2): 646–657.
- [21] Machado I P, Wit J D, Arnoldus J B, et al. Highly luminescent  $\text{Gd}_2\text{O}_2\text{S}: \text{Er}^{3+}, \text{Yb}^{3+}$  upconversion microcrystals obtained by a time- and energy-saving microwave-assisted solid-state synthesis[J]. *Journal of Alloys and Compounds*, 2023, 942: 169083.
- [22] 陈洋. 多维铒镱掺杂钒酸镥钆晶体的制备、结构与性能研究[D]. 青岛: 山东大学, 2023.  
Chen Y. Preparation, structure and properties of multidimensional erbium-ytterbium doped lutetium gadolinium vanadate crystals[D]. Qingdao: Shandong University, 2023.
- [23] 李洪波, 韩汝取, 李晓喜, 等. 双钙钛矿 $(\text{Y}, \text{Gd}, \text{Eu})\text{BaCo}_2\text{O}_{5+\delta}$ 的制备和氧敏感性[J]. *江苏科技大学学报(自然科学版)*, 2021, 35(5): 22–25, 58.  
Li H B, Han R Q, Li X X, et al. Synthesis and oxygen sensing properties of double perovskite  $(\text{Y}, \text{Gd}, \text{Eu})\text{BaCo}_2\text{O}_{5+\delta}$ [J]. *Journal of Jiangsu University of Science and Technology (Natural Science Edition)*, 2021, 35(5): 22–25, 58.
- [24] 刘晓妍, 李婷, 罗旭东, 等. 制备工艺对  $\text{La}_2\text{O}_3$  掺杂氧化镁陶瓷性能的影响[J]. *耐火材料*, 2022, 56(1): 34–37.  
Liu X Y, Li T, Luo X D, et al. Effects of preparation process on properties of  $\text{La}_2\text{O}_3$  doped magnesia ceramics[J]. *Refractories*, 2022, 56(1): 34–37.
- [25] Hernández-Adame L, Méndez-Blas A, Ruiz-García J, et al. Synthesis, characterization, and photoluminescence properties of  $\text{Gd}:\text{Tb}$  oxysulfide colloidal particles[J]. *Chemical Engineering Journal*, 2014, 258: 136–145.
- [26] Guo H, Zhang H, Wei R F, et al. Preparation, structural and luminescent properties of  $\text{Ba}_2\text{Gd}_2\text{Si}_4\text{O}_{13}:\text{Eu}^{3+}$  for white LEDs[J]. *Optics Express*, 2011, 19(102): A201–A206.
- [27] 王哲, 崔庚彦, 丁楠.  $\text{YPO}_4: \text{Ce}^{3+}, \text{Tb}^{3+}$ 反蛋白石光子晶体的制备及其发光性能的研究[J]. *光电子·激光*, 2022, 30(10): 1038–1042.  
Wang Z, Cui G Y, Ding N. Preparation and modified luminescence in  $\text{YPO}_4: \text{Ce}^{3+}, \text{Tb}^{3+}$  Inverse opal photonic crystals[J]. *Journal of Optoelectronics·Laser*, 2022, 30(10): 1038–1042.
- [28] 朱宪忠, 储成林.  $\text{Tb}^{3+}$ 在  $\text{Lu}_3\text{Ga}_5\text{O}_{12}$  中的光致发光性质及浓度猝灭机制[J]. *硅酸盐学报*, 2015, 43(7): 963–968.  
Zhu X Z, Chu C L. Photoluminescent properties and mechanism of concentration quenching of  $\text{Tb}^{3+}$  in  $\text{Lu}_3\text{Ga}_5\text{O}_{12}$ [J]. *Journal of the Chinese Ceramic Society*, 2015, 43(7): 963–968.
- [29] 欧奕意, 王笑军, 梁宏斌.  $\text{K}_3\text{La}(\text{PO}_4)_2$ 基质中  $\text{Tb}^{3+}$ 的发光和能量传递[J]. *发光学报*, 2022, 43(9): 1350–1360.  
Ou Y Y, Wang X J, Liang H B. Luminescence and energy transfer of  $\text{Tb}^{3+}$  in  $\text{K}_3\text{La}(\text{PO}_4)_2$ [J]. *Chinese Journal of Luminescence*, 2022, 43(9): 1350–1360.
- [30] 刘丹. 树枝状热活化延迟荧光材料的设计合成及光电性能研究[D]. 南京: 东南大学, 2021.  
Liu D. Synthesis and photoelectric property investigation of thermally activated delayed fluorescent dendrimers[D]. Nanjing: Southeast University, 2021.
- [31] Zhang B W, Zou H F, Guan H X, et al.  $\text{Lu}_2\text{O}_2\text{S}: \text{Tb}^{3+}, \text{Eu}^{3+}$  nanorods: Luminescence, energy transfer, and multicolour tuneable emission[J]. *CrystEngComm*, 2016, 18(39): 7620–7628.
- [32] Vijayakumar R, Venkataiah G, Marimuthu K. Structural and luminescence studies on  $\text{Dy}^{3+}$  doped boro-phosphate glasses for white LED's and laser application[J].

- Journal of Alloys & Compounds*, 2015, 652: 234–243.
- [33] 王孝东, 刘晓华, 陈绍军, 等.  $\text{CeO}_2\text{:Eu}^{3+}$ 粉末的溶胶-凝胶法制备及发光性能研究[J]. 光谱学与光谱分析, 2007, 27(11): 2182–2185.  
Wang X D, Liu X H, Chen S J, et al. Preparation of  $\text{CeO}_2\text{:Eu}^{3+}$  Powders by sol-gel method and their photoluminescence properties[J]. Spectroscopy and Spectral Analysis, 2007, 27(11): 2182–2185.
- [34] Wang F, Han Y, Lim C S, et al. Simultaneous phase and size control of upconversion nanocrystals through lanthanide doping[J]. *Nature*, 2010, 463: 1061–1065.
- [35] 叶建峰, 肖清泉, 秦铭哲, 等. Sc、Ce掺杂 $\text{CrSi}_2$ 的电子结构与光学性质的第一性原理[J]. *人工晶体学报*, 2021, 50(8): 1413–1421.  
Ye J F, Xiao Q Q, Qin M Z, et al. First-principles study on electronic structure and optical properties of Sc and Ce doped  $\text{CrSi}_2$ [J]. *Journal of Synthetic Crystals*, 2021, 50(8): 1413–1421.
- [36] 李逸, 冯庆, 张礼强, 等. 锐钛矿型氧化物 $\text{XO}_2$ (X=Ti, Sn, Zr, Ir)表面氧化性对 $\text{NH}_3$ 气体光学气敏传感特性的影响[J]. *原子与分子物理学报*, 2021, 38(5): 35–42.  
Li Y, Feng Q, Zhang L Q, et al. The effect of surface oxidation of anatase oxides $\text{XO}_2$ (X=Ti, Sn, Zr, Ir) on the characteristics of  $\text{NH}_3$  gas optical gas sensing[J]. *Journal of Atomic and Molecular Physics*, 2021, 38(5): 35–42.
- [37] 张富春, 张志勇, 张威虎, 等.  $\text{Pb}_x\text{Sr}_{1-x}\text{TiO}_3$ 的电子结构[J]. *物理化学学报*, 2009, 25(1): 61–66.  
Zhang F C, Zhang Z Y, Zhang W H, et al. Electronic structure of  $\text{Pb}_x\text{Sr}_{1-x}\text{TiO}_3$ [J]. *Acta Physico-Chimica Sinica*, 2009, 25(1): 61–66.
- [38] Som S, Mitra P, Kumar V, et al. The energy transfer phenomena and colour tunability in  $\text{Y}_2\text{O}_2\text{S}\text{:Eu}^{3+}\text{/Dy}^{3+}$  micro-fibers for white emission in solid state lighting applications[J]. *Dalton Transactions*, 2014, 43(26): 9860–9871.
- [39] Jia G, Song Y H, Yang M, et al. Uniform  $\text{YVO}_4\text{:Ln}^{3+}$ (Ln=Eu, Dy, and Sm) nanocrystals: Solvothermal synthesis and luminescence properties[J]. *Optical Materials*, 2009, 31(6): 1032–1037.
- [40] Bedekar V, Dutta D P, Mohapatra M, et al. Rare-earth doped gadolinia based phosphors for potential multicolor and white light emitting deep UV LEDs[J]. *Nanotechnology*, 2009, 20(12): 125707.
- [41] Gupta S K, Ghosh P S, Yadav A K, et al. Luminescence properties of  $\text{SrZrO}_3\text{/Tb}^{3+}$  perovskite: Host-dopant energy-transfer dynamics and local structure of  $\text{Tb}^{3+}$ [J]. *Inorganic Chemistry*, 2016, 55(4): 1728–1740.
- [42] Tian L, Shen J L, Xu T, et al.  $\text{Dy}^{3+}$  doped thermally stable garnet-based phosphors: Luminescence improvement by changing the host-lattice composition and Co-doping  $\text{Bi}^{3+}$ [J]. *RSC Advances*, 2016, 6(38): 32381–32388.
- [43] Liu C, Xia Z, Molokeev M S, et al. Synthesis, crystal structure, and enhanced luminescence of garnet-type  $\text{Ca}_3\text{Ga}_2\text{Ge}_3\text{O}_{12}\text{:Cr}^{3+}$  by codoping  $\text{Bi}^{3+}$ [J]. *Journal of the American Ceramic Society*, 2015, 98(6): 1870–1876.